Additive Manufacturing 48 (2021) 102414

Contents lists available at ScienceDirect

Additive Manufacturing

journal homepage: www.elsevier.com/locate/addma

Research paper

Effect of stress triaxiality and penny-shaped pores on tensile properties of laser powder bed fusion Ti-6Al-4V

Erik T. Furton [a], Alexander E. Wilson-Heid [a], Allison M. Beese [a,b,*]

[a] Department of Materials Science and Engineering, Pennsylvania State University, University Park, PA 16802, United States
[b] Department of Mechanical Engineering, Pennsylvania State University, University Park, PA 16802, United States

ARTICLE INFO

Keywords:
powder bed fusion
fracture
porosity
Ti-6Al-4V
stress triaxiality

ABSTRACT

In this study, the effect of internal penny-shaped pores on the strength and ductility of additively manufactured Ti-6Al-4V under uniaxial tension and notched tension loading was investigated. The behaviors of fully dense samples were compared to those of samples containing pores whose diameters ranged from 150 μm to 3000 μm within 6 mm diameter gauge regions. For uniaxial tension specimens, loss of strength occurred for samples containing pores larger than 870 μm (2.1% of the cross-sectional area), while ductility decreased for pores larger than 150 μm (0.07% of the cross-sectional area). The notched tension specimens – also with 6 mm diameter gauge regions and subject to greater stress triaxialities than uniaxial tension – were more severely affected by the pores; pores larger than 150 μm resulted in a reduction of strength, while all pore sizes significantly reduced ductility. Dense finite element simulations showed that plastic strain to failure was dependent on stress triaxiality in samples containing pores with a diameter of 540 μm (0.8% of the cross-sectional area) and smaller, while samples with larger pores failed with negligible plastic strain regardless of stress triaxiality. X-ray computed tomography showed negligible volumetric growth of pores for samples loaded to 75% of their displacement to failure.

1. Introduction

Because of its balance of strength, ductility, fatigue properties, and fracture toughness, Ti-6Al-4V is widely used for aerospace and biomedical applications [1]. However, conventional processing methods restrict the geometries that may be produced in Ti-6Al-4V, and as a means to reduce the restrictions on shape, significant research has been devoted to optimizing additive manufacturing (AM) processing of this alloy [2]. The focus of the present study is on laser powder bed fusion (L-PBF) AM of Ti-6Al-4V.

The L-PBF AM procedure introduces microstructural features absent in conventionally processed Ti-6Al-4V [2,3]. The fine, nonequilibrium morphology of AM microstructures results in higher strength and reduced ductility compared to conventionally processed Ti-6Al-4V [4]. One of the most significant factors affecting tensile properties in metals fabricated by AM is the presence of internal pores [5]. Different pore morphologies are characteristic of different processing parameter regimes, and may be generally classified as gas pores, keyhole pores, or lack-of-fusion (LOF) pores [6–8]. LOF defects result due to insufficient power density or inadequate melt pool overlap [9], and are characterized by their large size and sharp crack-like morphology, which introduce severe stress concentration factors that are detrimental to mechanical properties [9,10].

Meng et al. [11] analyzed the effect of built-in spherical pores in L-PBF Ti-6Al-4V for uniaxial tension specimens with 6.0 mm diameter gauge regions. It was found that spherical pores with diameters 500 μm (0.7% of the cross-sectional area) and smaller did not affect strength, but that ductility was reduced with pores 1000 μm in diameter (2.8% of the cross-sectional area). Wilson-Heid et al. [12] analyzed the impact of penny-shaped pores in austenitic stainless steel 316L (SS316L) uniaxial tension specimens with 6.0 mm diameter gauge regions and showed that ductility was more sensitive to internal pore diameter than ultimate tensile strength (UTS). Pores 600 μm (1.0% of the cross-sectional area) and larger reduced ductility while UTS was only affected by pores 2400 μm (16.0% of the cross-sectional area) and larger. In materials with low strain hardening – such as Ti-6Al-4V and SS316L – ductility is more severely affected than UTS because at large plastic strains, the flow stress is nearly independent of strain [13]. At large strains, strength is insensitive to premature fracture; only pores large enough to induce fracture prior to the exhaustion of strain hardening reduce UTS.

* Corresponding author at: Department of Materials Science and Engineering, Pennsylvania State University, University Park, PA 16802, United States.
E-mail address: amb961@psu.edu (A.M. Beese).

https://doi.org/10.1016/j.addma.2021.102414
Received 31 August 2021; Received in revised form 5 October 2021; Accepted 18 October 2021
Available online 21 October 2021

Table 1
Minimum and maximum permissible composition of Ti-6Al-4V powder in wt%.

	Ti	Al	V	Fe	O	C	N	H	Y
Min	Bal.	5.50	3.50	–	–	–	–	–	–
Max	Bal.	6.75	4.50	0.30	0.20	0.08	0.05	0.015	0.005

In addition to microstructure and porosity, fracture behavior is also influenced by stress state [14]. A frequently used scalar metric to describe the stress state is the stress triaxiality, which is a measure of the ratio of hydrostatic to deviatoric stress, i.e., the ratio between the mean normal stress (σ_m) and the von Mises stress (σ_{vm}):

$$\eta = \frac{\sigma_m}{\sigma_{vm}} \tag{1}$$

In ductile materials, increased triaxiality reduces ductility as negative pressure drives, or accelerates, crack and pore growth. In conventionally processed Ti-6Al-4V, high triaxialities are associated with brittle cleavage fracture while low triaxialities are associated with ductile void nucleation and growth [15]. Notched tension (NT) specimens, which have bidirectional curvature resulting in a gradually reduced cross section at the center of the specimen (see Fig. A1), allow for the targeted probing of the effect of increased stress triaxiality on mechanical properties. During tensile loading, the curvature induces hydrostatic stress, for which the approximate stress triaxiality is obtained with the Bridgman formula [16]:

$$\eta \approx \frac{1}{3} + ln\left(1 + \frac{a}{2R}\right) \tag{2}$$

where a is the radius of minimum cross-section and R is the notch radius.

This study sought to experimentally determine the impact of internal defect size and stress triaxiality on the mechanical behavior of L-PBF Ti-6Al-4V. A single penny-shaped pore was intentionally incorporated at each of the otherwise fully dense specimens' centers to model LOF defects. The samples were fabricated in uniaxial tension (UT) and three NT geometries and designed to probe a range of stress triaxialities from ~0.3–1.0. Through mechanical testing, the relative critical pore sizes were identified for which loss in strength and ductility occurred. Finite element simulations of dense specimens provided information about the strain and stress state and, coupled with experimental results, identified the impact of defect size on the equivalent plastic strain to failure for a range of stress triaxiality values. A secondary objective was to identify the volumetric change of the pores after loading samples to 75% of their displacement to failure. X-ray computed tomography (XCT) was used to image samples before and after deformation, showing that with this amount of applied macroscale deformation, the pores had little to no increase in volume regardless of initial pore size or stress triaxiality. This study provides insight to aid establishment of acceptance criteria for evaluation of structural AM components under static loading [17], whereby if no pore exceeding a relative critical size – determined as a function of expected stress state at that location – is detected, a component could pass acceptance criteria and find use in load-bearing applications.

2. Experimental methods

2.1. Sample fabrication

Samples were fabricated with a 3D Systems ProX DMP 320L-PBF machine with a mixture of Grade 5 recycled powder and virgin powder. The powder diameters ranged from 15 μm to 45 μm with the composition given in Table 1 [18]. The following processing parameters were selected to produce dense specimens: laser scan speed of

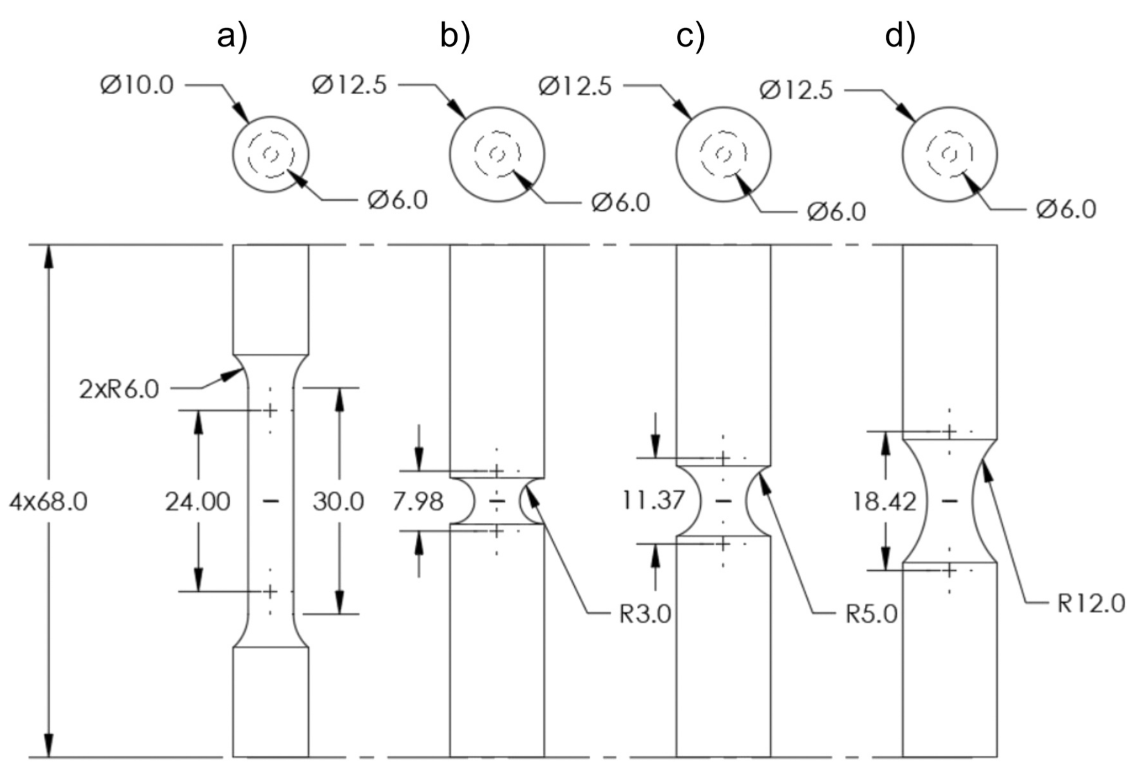

Fig. 1. Sample geometries for (a) uniaxial tension, (b) R3 notched tension, (c) R5 notched tension, and (d) R12 notched tension. Intentional pores at centers are pictured for reference. Crosshairs show where virtual extensometer endpoints were located. All dimensions are in mm.

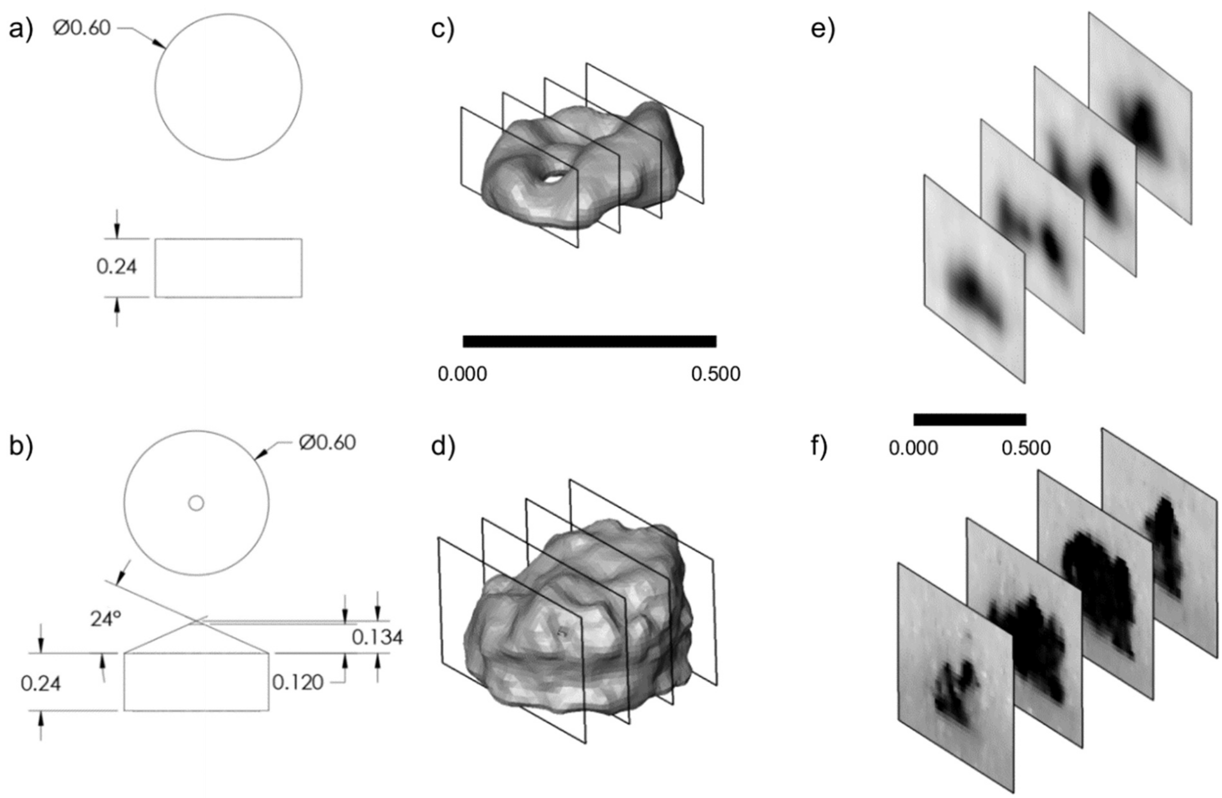

Fig. 2. Dimensions of 600 μm pore (a) without conical feature and (b) with conical feature. X-ray CT reconstruction of 600 μm pore (c) without conical feature and (d) with conical feature to prevent pore collapse due to dross formation. Grayscale cross-sections of pore (e) without conical feature and (f) with conical feature. All dimensions are in mm.

1300 mm/s, laser power of 250 W, and layer height of 60 μm. After fabrication, the samples were heat treated by Solar Atmospheres at 650 °C for 3 h and then cooled in an argon environment. Before testing, the densities of the samples were evaluated using Archimedes measurements using an Ohaus Explorer Pro 613 balance.

2.2. Sample design

Uniaxial tension (UT) samples were designed in compliance with the ASTM E8 standard [19]. Notched tension bars with notch radii of 3 mm (R3NT), 5 mm (R5NT), and 12 mm (R12NT) were also fabricated. All samples were individually fabricated as 68 mm tall cylinders, with diameters of 10.0 mm and 12.5 mm for the uniaxial tension and notched tension specimens, respectively. In a secondary process step, gauge regions were machined to designed testing dimensions with a computer numerical control (CNC) lathe. For all geometries (shown in Fig. 1), the minimum cross-sectional diameter was 6.0 mm.

In the computer-aided design (CAD) models, a penny-shaped pore was intentionally designed at the center of each specimen. During fabrication, the laser executed two concentric passes around the intentional pores, resulting in the lack of fusion within the designated porous volume. Although loose powder was present within these intentional pores, the loose powder did not influence the mechanical behavior. For both uniaxial and notched geometries, pores were built with designed diameters of 300 μm, 450 μm, 600 μm, 900 μm, 1200 μm, 1800 μm, and 2400 μm. For UT specimens only, samples containing 3000 μm pores were built. Fully dense specimens without any intentional pores were also fabricated. Three specimens with each pore size and geometry were fabricated and tested to determine variability, with the exception of the fully dense UT sample and the two pore-height study samples (see last paragraph of this section), for which two samples were tested.

Initially, the pore geometry was designed to be perfectly cylindrical (Fig. 2a). However, due to the overhang of the cylinder's upper face, dross formation led to fusing between the upper and lower surfaces of the cylinder, resulting in pore closure. To reduce pore closure effects, a conical feature was appended to the top surface of the cylinder (Fig. 2b). The cone was designed to slope upwards at a 24° angle, and the upper 10% of the cone's height was flattened to prevent the formation of a sharp, singular point (e.g., for the cone with a 0.134 mm height presented in Fig. 2b, the topmost 10% - 0.014 mm – was flattened). Representative X-ray CT images of the effect of a conical feature,

Table 2
Designed versus measured pore diameter, where the diameters were measured using XCT of witness samples.

Designed diameter [μm]	Measured diameter [μm]	Relative difference in diameter [-]	Designed fraction of cross-section [%]	Measured fraction of cross-section[%]	Relative difference in fraction of cross-section[-]
300	153 ± 26	-49%	0.25%	0.07% ± 0.02%	-74%
450	374 ± 11	-17%	0.56%	0.39% ± 0.02%	-31%
600	536 ± 21	-11%	1.0%	0.8% ± 0.1%	-20%
900	874 ± 20	-3%	2.3%	2.1% ± 0.1%	-6%
1200	1193 ± 15	-1%	4.0%	4.0% ± 0.1%	-1%
1800	1807 ± 36	0%	9.0%	9.1% ± 0.4%	1%
2400	2391 ± 22	0%	16.0%	15.9% ± 0.3%	-1%
3000	2992 ± 16	0%	25.0%	24.9% ± 0.3%	-1%

Table 3
Parameters used in DIC data collection and analysis.

Hardware		Software	
Camera	Point Grey GRAS-50S5M-C	DIC software	Correlated solutions VIC-3D 9[20]
Lens	Fujinon HF75SA-1	Subset Size	29 px (0.71 mm)
Focal Length	75 mm	Step Size	7 px (0.17 mm)
Image Scale	41 px/mm	Subset Shape Function	Affine
Image Resolution	2048 px × 2448 px	Quantity of Interest	Displacement
Field of View	50 mm × 60 mm	Correlation Criterion	Normalized Squared Differences
Stand-off Distance	570 mm	Subset Weights	Gaussian
Stereo Angle	20°	Strain Formulation	Lagrangian
Acquisition Rate	1 Hz		
Patterning Technique	White basecoat, black spray paint		
Pattern Feature Size	~0.1 mm		

showing 600 μm diameter pores, are presented in Fig. 2c-f. By reducing stochastic pore closure effects, consistent, repeatable pore geometries were fabricated.

Two witness samples, which each contained one of each size intentional pore were imaged with XCT (see Section 2.5). A total of 180 Feret diameter measurements were taken 1° apart for each pore size. Uncertainty was calculated from both the distribution of ferret diameters for an individual specimen and variability in measured diameter between the two witness samples. The measured pore diameters are compared to the designed pore diameters in Table 2. For pores intended to be 1200 μm and larger, the measured pore diameters were within 1% of the designed diameter. With decreasing pore size, the measured pore diameters were undersized. In the remainder of the paper, pores indented to be 300, 450, 600 and 900 μm in diameter shall be referred to as 150, 370, 540, and 870 μm pores, respectively.

For penny-shaped pores, the pore height was an unconstrained design parameter. To verify that the pore height did not play a critical role in mechanical behavior, a parametric study was performed, with pore diameter held constant at 540 μm: two specimens with 180 μm tall (3 layers), three specimens with 240 μm tall (4 layers), and two specimens with 300 μm tall (5 layers) intentional pores were fabricated. There was no significant impact of pore height on strength or ductility, and the remainder of the samples were all designed to have pore heights of 240 μm (4 layers); further details are presented in Table 6.

2.3. Mechanical testing

Mechanical testing was performed using an MTS Criterion Model 45 load frame with a 150 kN load cell. Tensile tests were performed to failure using a crosshead displacement rate of 0.007 mm/s. The gauge lengths varied for different sample geometries and resulted in different strain rates, but all were on the order of 10^{-4}/s. Of the three samples manufactured with each geometry and pore size, two were monotonically loaded until failure, and the third was loaded until approximately 75% displacement to failure, and then unloaded at a crosshead displacement rate of 0.020 mm/s. A select number of samples were scanned with XCT both as-received and after unloading; details are discussed in Section 2.5.

Force data were obtained directly from the MTS Criterion Model 45 Universal Test System, while displacement data were obtained by stereographic digital image correlation (DIC). DIC parameters are presented in Table 3. Displacements were measured with virtual extensometers, with lengths of 24.00 mm, 7.98 mm, 11.37 mm, and 18.42 mm for the UT, R3NT, R5NT, and R12NT specimens, respectively (Fig. 1).

The notched tension specimens experienced little plastic deformation, and therefore the elastic deformation contributed a significant proportion of the total deformation to failure. Due to the small total strain/deformation, data in the elastic regime were obtained by compliance calculations, while displacement data in the plastic regime were obtained with DIC.

2.4. Finite element modeling

Finite element models were created to model the fully dense UT, R3NT, R5NT, and R12NT specimens using ABAQUS 2018 [21]. All simulations were performed on dense models, regardless of whether they were being used to simulate tests with or without pores; after fabrication of engineering components, in cases where flaws are known to be present, nondestructive evaluation may establish an upper limit for flaw size but the size and location of defects are often not known. Therefore, the models did not explicitly incorporate pores but instead considered fully dense specimens. The experimentally determined effect of porosity on displacement to behavior was correlated to the computationally determined strain and stress state. The fully dense finite element simulations were terminated at these displacements to failure. This method allows a direct comparison of specimens with pores to fully dense parts and, by assuming a preexisting defect pore size, identifies the limitations in the material response. Detailed information on the finite element models is presented in Appendix A.

The material model was adopted from ref. [22]. The model used the Hill48 yield criterion, an associated flow rule, and an isotropic Swift hardening law, which is given as:

$$\Delta\sigma_y = \left\{ \begin{array}{ll} nA(\varepsilon_o + \varepsilon^p)^{n-1} & \text{for} \quad \varepsilon^p \le 0.038, \\ K\Delta\varepsilon^p & \text{for} \quad \varepsilon^p > 0.038 \end{array} \right\} \tag{3}$$

where the flow stress σ_y is a function of the equivalent plastic strain ε_p and the experimentally determined coefficients n, A, ε_o, and K. The calibrated parameters for L-PBF Ti-6Al-4V are given in Table 4.

Table 4
Material model parameters used in finite element models.

		Hill 48 parameters						Swift law parameters			
Elastic modulus[GPa]	Poisson's ratio[-]	F[-]	G[-]	H[-]	L[-]	M[-]	N[-]	A[MPa]	n[-]	ε_o[-]	K[MPa]
114	0.3	0.465	0.535	0.465	1.450	1.500	1.450	1349	0.042	0.002	950

Table 5
Archimedes Density measurements and calculated porosity assuming a density of 4.42 g/cm^3 for Ti-6Al-4V.

	UT	R3NT	R5NT	R12NT
Density [g/cm^3]	4.411 ± 0.005	4.419 ± 0.001	4.419 ± 0.002	4.419 ± 0.001
Density [%]	99.79 ± 0.11%	99.98 ± 0.02%	99.98 ± 0.03%	99.97 ± 0.03%
Dense Volume [mm^3]	1869	2942	2863	2737

Table 6
Pore height versus UTS and strain to failure for the parametric study on impact of pore height on mechanical behavior.

Layers	Height	UTS	Strain to fracture
[-]	[μm]	[MPa]	[-]
3	180	1206 ± 12	0.074 ± 0.006
4	240	1210 ± 6	0.078 ± 0.008
5	300	1205 ± 4	0.086 ± 0.003

Fracture was assumed to initiate from each model's centermost element. A mesh convergence study was performed on all sample geometries with central element edge lengths of 0.160 mm, 0.080 mm, 0.040 mm, and 0.020 mm. The evolution of Hill 48 equivalent plastic strain and stress triaxiality were compared amongst the different models. For all model geometries, the representative element's response was deemed converged with a 0.040 mm edge length, as further reduction in element size did not affect stress triaxiality and equivalent plastic strain by more than 1%. Therefore, the 0.040 mm mesh was used for all further analysis.

2.5. X-ray computed tomography

XCT was performed using a General Electric v=tome|x L300 nano/microCT machine with a voltage of 170 kV and current of 55 mA. Each sample was placed 35 mm from the source, and the detector was located 700 mm from the sample, which was shielded with a 0.5 mm copper sheet. The detector's pixel pitch was 200 μm. Each sample was rotated at 0.4° increments, and 900 images were taken with an exposure time of 1000 ms for each image. The projected images were reconstructed using phoenix datos | x 2.0 CT software, with voxel edge lengths of 10.0 μm.

Pore segmentation and analysis were performed with Avizo 2020.2 (Thermo Fisher Scientific). The threshold for pore identification was

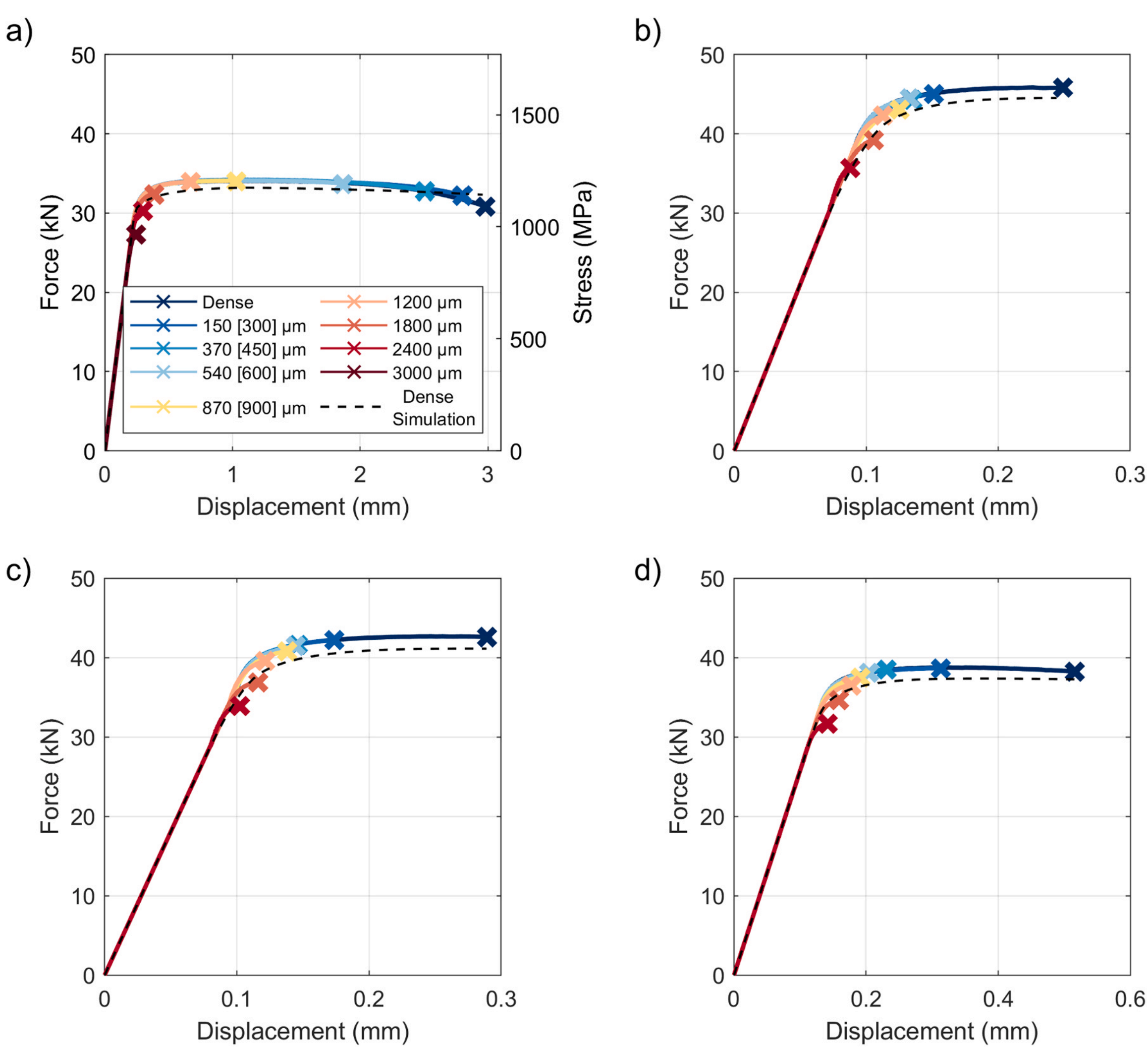

Fig. 3. Experimental and dense finite element simulation force-displacement curves, (a) uniaxial tension, (b) R3NT, (c) R5NT, and (d) R12NT (color online). For clarity, the abscissa scales are not consistent between plots. In the legend, measured pore diameters are shown, with designed pore diameters in brackets.

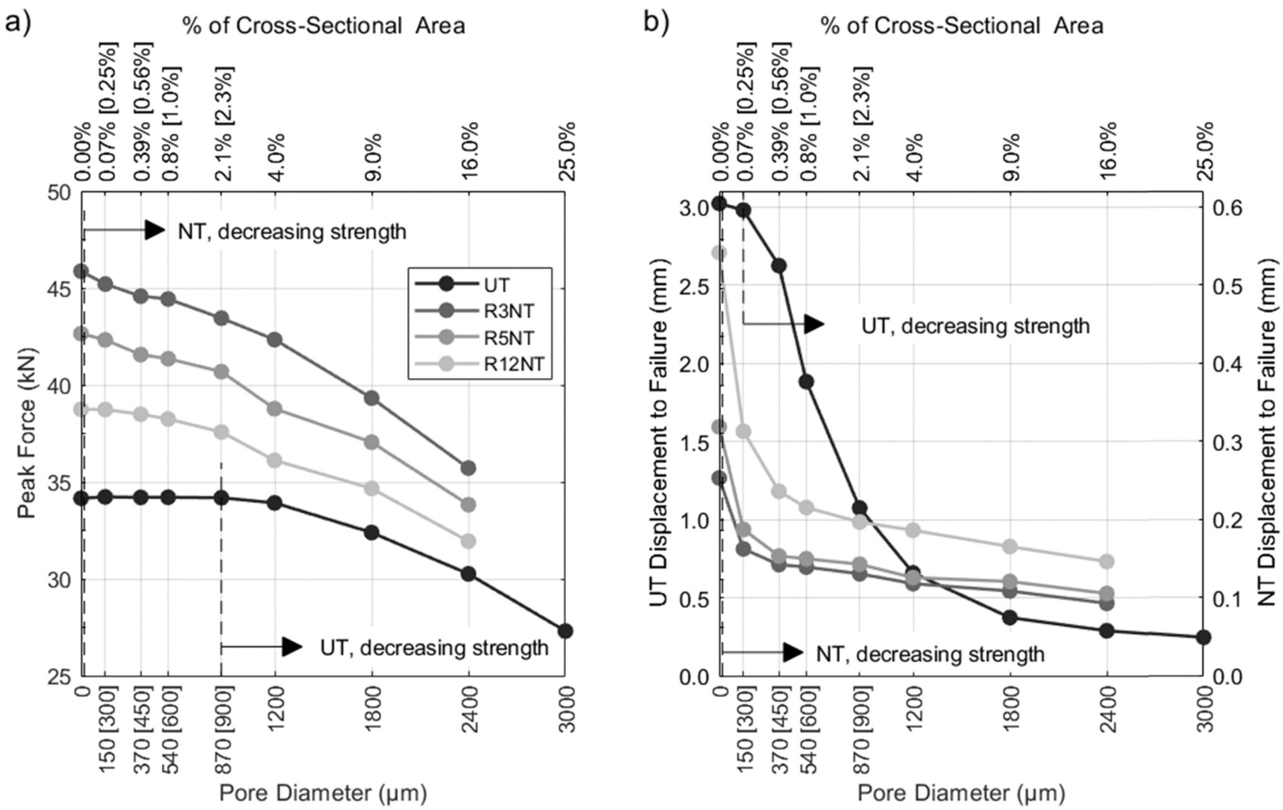

Fig. 4. (a) Peak force as a function of pore diameter, and (b) displacement to failure as a function of pore diameter. For clarity, the displacement data are presented with two ordinate scales; the left applies to UT specimens, while the right applies to R3NT, R5NT, and R12NT specimens. Data are presented for the measured pore diameters, with designed pore diameters in brackets.

three times the voxel size [23], and therefore pores required edge lengths exceeding 30 μm to be deemed detectable.

XCT scans were performed for UT specimens with pores (150 μm, 370 μm, 540 μm, 870 μm, 1200 μm, and 1800 μm pore diameters) as well as NT specimens (dense and those containing 150 μm, 540 μm, and 1200 μm pores). Scans were performed both before initial loading and after deforming up to approximately 75% of the displacement to failure to determine the effect of applied deformation on pore growth.

3. Experimental results and discussion

3.1. Archimedes density

Archimedes density measurements revealed that all samples were at least 99.8% dense, as shown in Table 5, assuming a density of Grade 5 Ti-6Al-4V of 4.42 g/cm^3 [24]. The variability for notched tension specimens was smaller than for UT specimens because they were approximately 50% larger in sample volume and therefore less sensitive to measurement uncertainty.

The effect of the intentional pore's size on Archimedes density was negligible. A fully dense UT bar's volume was 1869 mm^3 (Table 5). The largest intentional pore – the 3000 μm pore – had a designed volume of 3.3 mm^3. Thus, the theoretical effect of the largest pore would be a 0.2% change in density – 0.008 g/cm^3 – which was comparable to one standard standard error of the mean of three density measurements. The Archimedes density measurement was not precise enough to isolate the presence of the intentional pores over statistical noise.

The Archimedes density measurements were validated by comparison to XCT data of fully dense material. For a 1.5 mm tall section of nominally dense material from each specimen geometry, XCT measurements indicated a porosity ranging from $0.0003 \pm 0.0002\%$ to $0.0019 \pm 0.0011\%$, where nearly 100% density was consistent with the Archimedes measurements.

3.2. Mechanical testing results

The strength and ductility values from the pore height parametric study are presented in Table 6. The UTS for all tests were within 1% of one another. The strain at fracture had larger variability, but there was no statistically significant difference between means (p-value of 0.13 between 3-layer and 5-layer samples). It was concluded that the pore height parameter did not impact the tensile response within the ranges studied.

Representative force versus displacement curves are presented in Fig. 3, along with the superimposed dense finite element simulation results. Loads and displacements, rather than engineering stresses and strains, are presented because in NT samples the cross-section varies and therefore neither stress nor strain is homogenous across the entire sample gauge region. With the exception of the fully dense specimens and a single UT sample with a 370 μm pore (0.4% cross-sectional area), all samples fractured at the pore. Increased stress triaxiality corresponded with increased maximum load and decreased ductility, which is

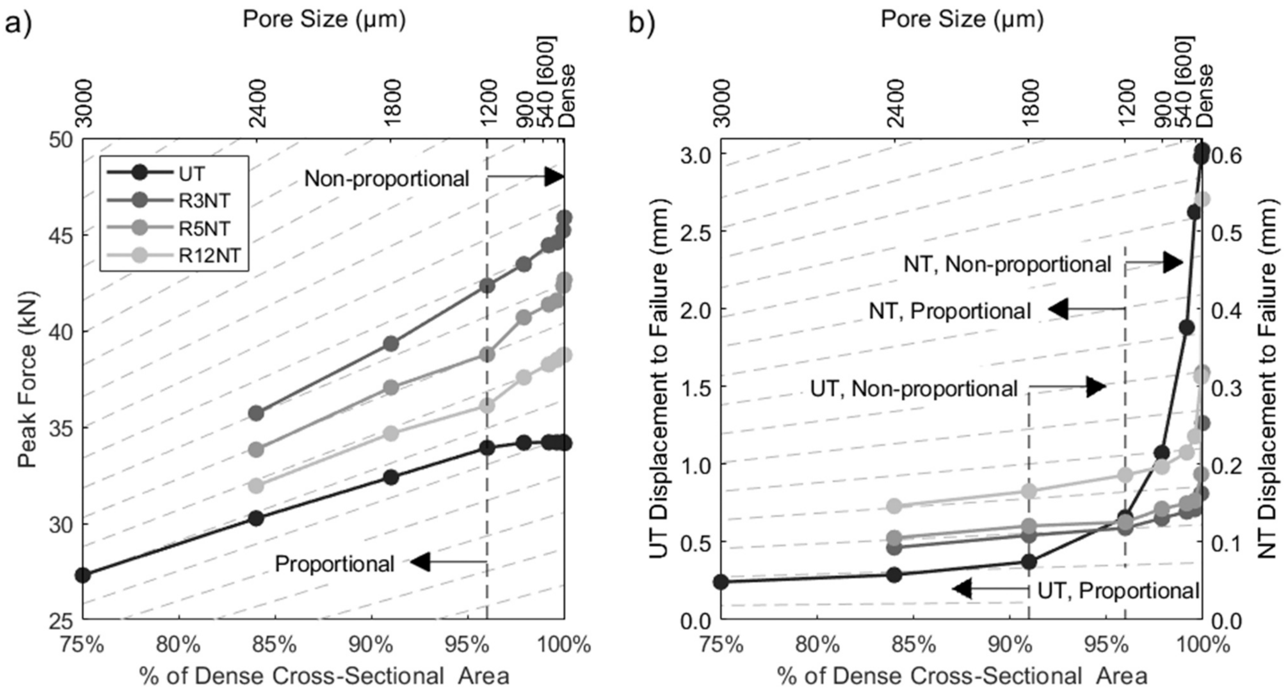

Fig. 5. (a) Peak force and (b) displacement to failure as functions of remaining dense cross-sectional area. For clarity, the displacement data are presented with two ordinate scales; the left applies to UT specimens, while the right applies to R3NT, R5NT, and R12NT specimens. Dashed lines emanating from origin represent proportionality. Data are presented for the measured pore diameters, with designed pore diameters in brackets.

consistent with conventionally processed metals [15,24]. For a given geometry, consistent overlap of force-displacement curves for the different pore sizes was observed, the only difference that increased pore size induced fracture sooner. Additionally, there was good agreement between experimental results and dense simulation data.

The effect of pore diameter on peak load and displacement to failure is presented in Fig. 4. For UT samples, strength was tolerant of defects 870 μm (2.1% cross-sectional area) or smaller. For NT specimens, from the introduction of a 150 μm pore (0.07% cross-sectional area) to the largest pore (3000 μm pore, 25% cross-sectional area), the maximum load-carrying capability continually decreased with increasing pore size.

The impact of pore size on displacement to failure was more severe than its effect on peak load. For UT specimens, beyond a pore size of 150 μm (0.07% cross-sectional area), the displacement to failure precipitously dropped, with a decrease in 61% of the ductility compared to the sample containing a 870 μm pore. NT specimens were even more significantly impacted by the presence of an internal pore; compared to the fully dense specimens, the specimens with a 150 μm pore lost 40% of their ductility.

To investigate the effect of pore size on peak load, experimental data were compared with a model that assumes peak load is proportional to the minimum dense cross-sectional area. In the limiting case of zero dense cross-sectional area, the specimen's load carrying capacity becomes zero; with increasing cross-sectional area, the load-bearing

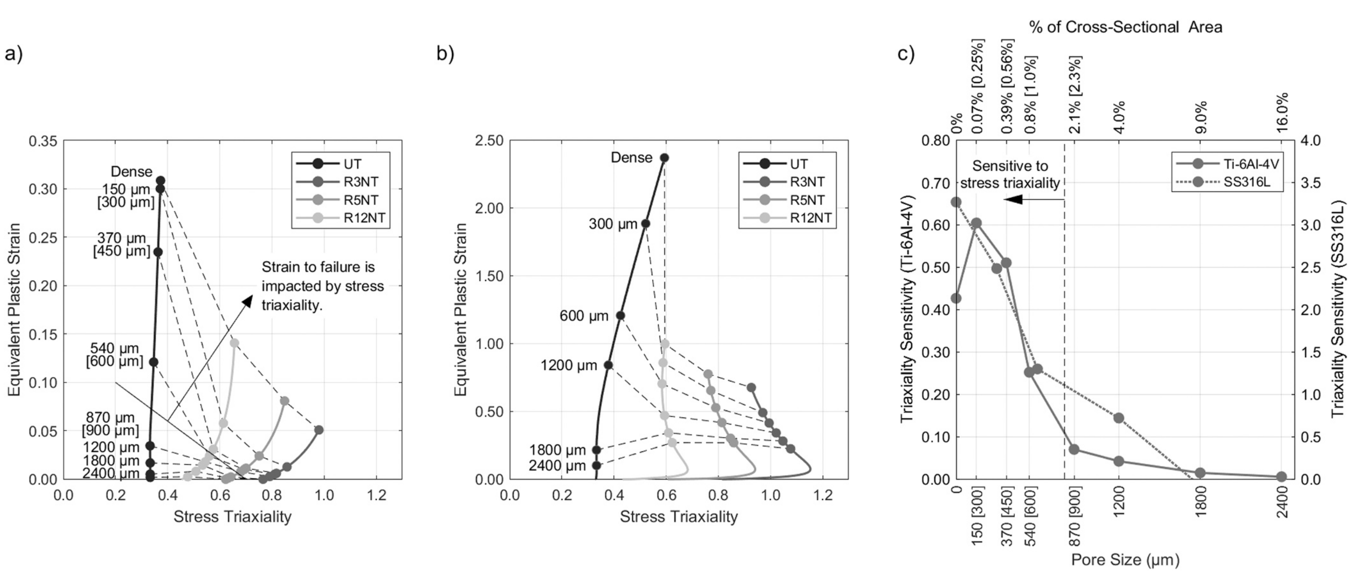

Fig. 6. Mean stress triaxiality versus equivalent plastic strain in L-PBF (a) Ti-6Al-4V (this study) and (b) 316L (from ref. [25]), and (c) triaxiality sensitivity for both Ti-6Al-4V and SS316L. For clarity, the triaxiality sensitivities for Ti-6Al-4V and SS316L are presented on two different ordinate scales. Data are presented for the measured pore diameters, with designed pore diameters in brackets.

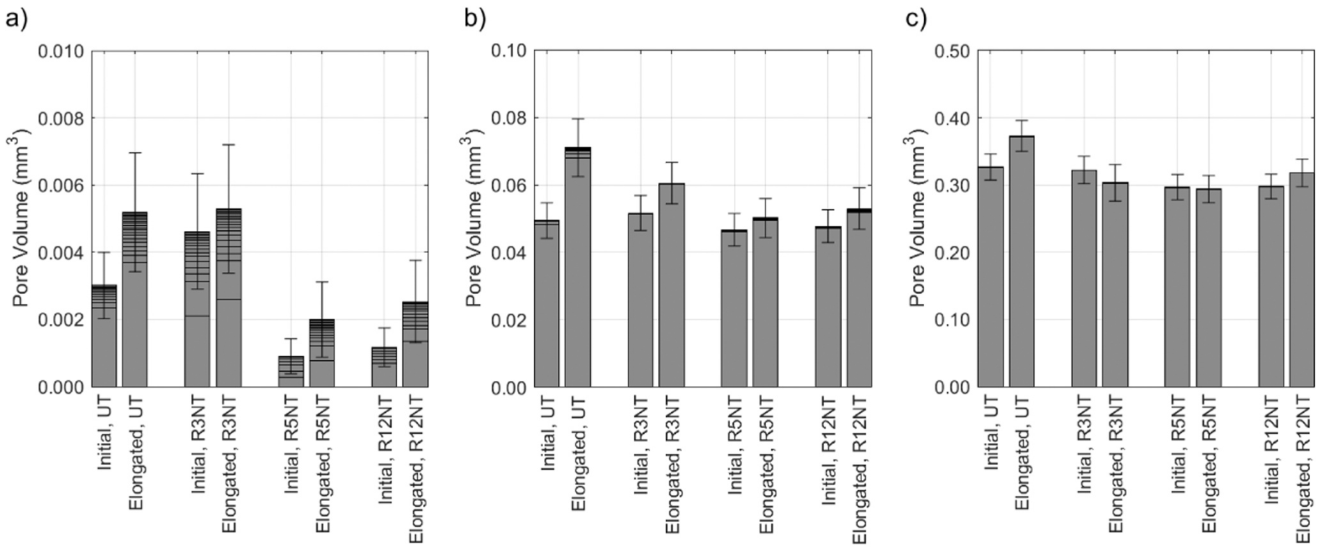

Fig. 7. Pore volumes before and after load-unload cycle, for initial pore sizes of (a) 150 µm, (b) 540 µm, and (c) 1200 µm. Horizontal bars delineate the contribution of each individual pore.

capability is assumed to linearly increase:

$$F_{peak} = q \times \frac{A_{remaining \quad cross-section}}{A_{dense \quad cross-section}} \tag{4}$$

where q is an undetermined coefficient. A similar relation between ductility and dense cross-sectional area was formulated.

In Fig. 5, the peak force and elongation to failure are measured against the remaining cross-sectional area. Lines emanating from origin represent the proportional behavior assumed in Eq. (4). When experimentally obtained data lie parallel to the proportionality lines, loss in strength or ductility may be ascribed to a failure mechanism that is governed by a loss in cross-sectional area. When the experimentally obtained data deviate from the proportionality lines, nonlinear effects are implied.

In Fig. 5a, for both UT and NT samples with less than 96% dense cross-sectional area (1200 µm pore), the peak force was proportional to dense cross-sectional area, meaning strength was limited by the lack of cross-sectional area. With cross-sectional density increasing over 96%, the UT samples experienced no further increase in strength due to the onset of plastic deformation. Nonlinearity in NT samples was the opposite: compared to a dense sample, the presence of a small pore in a NT sample disproportionally reduced the load carrying capability compared to the loss in cross-sectional area.

Similar conclusions may be drawn from the ductility measurements in Fig. 5b, where the elongation to failure is compared against the remaining cross-sectional area. For UT geometries, the elongation to failure was proportional until 91% (1800 µm pore), while for NT geometries, the elongation to failure was proportional until 96% (1200 µm pore). Above the proportionality cutoffs, the loss in ductility was more rapid than the loss in cross-sectional area.

3.3. Effect of stress triaxiality and pore size on equivalent plastic strain to failure

Finite element analysis was performed by simulating the tensile deformation of dense samples to the experimental elongation to failure for samples with pores. The evolution of equivalent plastic strain and stress triaxiality were extracted from the centermost element. To account for non-proportional loading, the mean stress triaxiality, η_{mean}, with respect to plastic strain, ε_p, is considered, where:

$$\eta_{mean} = \frac{1}{\varepsilon_{p,fracture}} \int_0^{\varepsilon_{p,fracture}} \eta d\varepsilon_p \tag{5}$$

The interaction between pore size, mean stress triaxiality, and equivalent plastic strain to failure is given in Fig. 6a. For Ti-6Al-4V, with pores 540 µm (0.8% of cross-sectional area) and smaller, the ductility was strongly dependent on stress triaxiality.

For the R3NT, R5NT, and R12NT specimens, the equivalent plastic strain to failure from dense specimens to specimens with a 370 µm pore decreased between 78% (R12NT) and 88% (R3NT). For the case of UT, the equivalent plastic strain to failure only decreased 24% for the same size pore relative to dense specimens. The large difference in ductility suggests that stress triaxiality values above 0.4 amplify the effect of internal pores on failure.

The impact of stress triaxiality on plastic strain to failure for a given pore size was quantified by fitting least-squares linear regressions through data points of the same pore size across all specimen geometries (Fig. 6a). The negative of the slope represents the mean change in plastic strain to failure with respect to the change in stress triaxiality for a given pore diameter. This metric is called the triaxiality sensitivity in the remainder of this section, and is presented in Fig. 6c as a function of pore size. The triaxially sensitivity was positive because increased stress triaxiality reduced the strain to failure.

For Ti-6Al-4V, for pore diameters of 870 µm (2.1% cross-sectional area) and larger, the triaxiality sensitivity was 0.07 or less, and there was only a slight dependance of equivalent plastic strain on triaxiality; for all triaxialities, fracture occurred at nearly the onset of plastic strain. For pore sizes 540 µm (0.8% cross-sectional area) and smaller, the stress triaxiality played a key role in ductility, with the magnitude of triaxiality sensitivity at least 0.25.

The effect of stress triaxiality on equivalent plastic strain in L-PBF Ti-6Al-4V is compared to that of SS316L [25] (Fig. 6b). SS316L is a significantly more ductile material, as the tensile ductility in L-PBF SS316L is 64% [12] compared to 13% in the L-PBF Ti-6Al-4V reported here. Pores were more impactful in the less ductile Ti-6Al-4V: for the R3NT geometries, the introduction of a 150μm diameter pore reduced plastic strain by 75%, 70%, and 59% in Ti-6Al-4V for the R3NT, R5NT, and R12NT geometries, respectively. Correspondingly in SS316L, the equivalent plastic strain to failure only decreased by 29%, 16%, and 16% for a similarly sized pore and the same test geometries. However, SS316L was affected more by triaxiality, where the magnitude of triaxiality sensitivity for pores 600 μm and smaller exceeded 1.3, compared to 0.25 for Ti-6Al-4V (Fig. 6c).

3.4. Characterization of pores with XCT

The total pore volumes measured with XCT are presented in Fig. 7 both before tensile testing and after loading to 75% of the elongation to failure. Error bars were calculated by multiplying the measured surface area with a voxel uncertainty factor. Ref. [26] states that the voxel uncertainty factor can be as low as 0.1 voxels for optimal thresholding methods, but a comparison of independent measurements made by three analysts in the present study identified the repeatability to be 0.56 voxels. The horizontal bars delineate the volumetric contribution from individual pores; for the 150 μm pore samples, in addition to the intentional pore, many small unintentional pores contributed significant volume. For samples containing large pores, such as the 1200 μm pore samples, only the intentional pore contributed significant volume.

For all pores analyzed with XCT, there was nearly zero volumetric growth regardless of pore size or stress triaxiality with the exception of the UT, 600 μm pore sample. Unlike the observation of significant volumetric expansion for pores in L-PBF SS316L after loading and prior to fracture as reported in ref. [25], the dominant failure mechanism in Ti-6Al-4V is not attributable to the intentional pore's volumetric expansion.

4. Summary and conclusions

The effects of pore size and stress triaxiality on the strength and ductility of L-PBF Ti-6Al-4 V were investigated by embedding penny-shaped pores into UT and NT mechanical test specimens. This study's primary conclusions are:

- In UT specimens, pores smaller than 870 μm (2.1% of the cross-sectional area) did not affect the ultimate tensile strength, whereas for NT specimens, ultimate tensile strength monotonically decreased with the presence of the pore and increasing pore size.
- Once the pore diameter exceeded 870 μm (2.1% of the cross-sectional area), the strength scaled proportionally with cross-sectional area for both UT and NT specimens.
- Elongation to failure was more sensitive to porosity than strength. Once the pore diameter exceeded 150 μm (0.07% of the cross-sectional area) for UT specimens, significant reduction in ductility occurred. NT specimens were more sensitive to porosity, with a loss of 40% of ductility for specimens containing 150 μm pores compared to fully dense specimens.
- For pore sizes larger than 540 μm (0.8% of the cross-sectional area), the plastic strain to failure was small and largely unaffected by stress triaxiality, while for smaller pores the strain to failure was highly dependent on stress triaxiality. NT samples were more severely affected by pores than UT samples, with a reduction of 78–88% strain to failure due to a 150 μm pore (0.07% of the cross-sectional area), compared to 24% reduction for UT samples.
- XCT measurements before and after loading to 75% of the elongation to failure did not identify volumetric pore growth with this amount of loading.

CRediT authorship contribution statement

Erik Furton: Formal analysis, Methodology, Visualization, Investigation, Software, Validation, Data curation, Writing – original draft. **Alexander Wilson-Heid:** Investigation. **Allison Beese:** Conceptualization, Methodology, Resources, Supervision, Project administration, Funding acquisition, Writing – review & editing.

Declaration of Competing Interest

The authors declare that they have no known competing financial interests or personal relationships that could have appeared to influence the work reported in this paper.

Acknowledgements

The financial support provided by the National Science Foundation through award number CMMI-1652575 is gratefully acknowledged. Any opinions, findings, and conclusions or recommendations expressed in this material are those of the authors and do not necessarily reflect the views of the National Science Foundation. The authors are grateful to the staff of the Center of Quantitative Imaging (CQI) at Penn State for their assistance in obtaining XCT data. The authors are grateful for Isabelle Seidenberg's assistance in XCT analysis for uncertainty quantification.

Appendix A

Detailed discussion of the finite element models is presented below. Isometric views of all model geometries are shown in Fig. A1. The models were comprised entirely of C3D8R linear hexahedral reduced integration elements.

For all geometries, the boundary conditions included a vertical constraint on the lower surface and an enforced vertical displacement of the upper surface. Only half of each specimen was modeled to reduce computation times, and a symmetry condition was applied to the lateral face.

To further reduce computational time, the meshes were each divided into three separate regions with differing mesh densities. Each region was joined to neighbors with tie constraints. Farthest away from the model's center, a coarse mesh was composed of elements with typical edge lengths of 0.30 mm. In the gauge regions, the mesh was refined so the typical element edge length was 0.10 mm. Finally, a mesh refinement study was performed on the centermost region, and concluded that convergence resulted from elements with a typical edge length of 0.04 mm.

Similar to digital image correlation, displacements were recorded by measuring the evolution of distance between two surface nodes. The initial distance between the two nodes were located 24.00 mm, 7.98 mm, 11.37 mm, and 18.42 mm apart for the UT, R3NT, R5NT, and R12NT models, respectively. The gauge dimensions were identical to those used in DIC (Fig. 1).

The strain and stress state were extracted from the centroid of the centermost element (Fig. A1i).

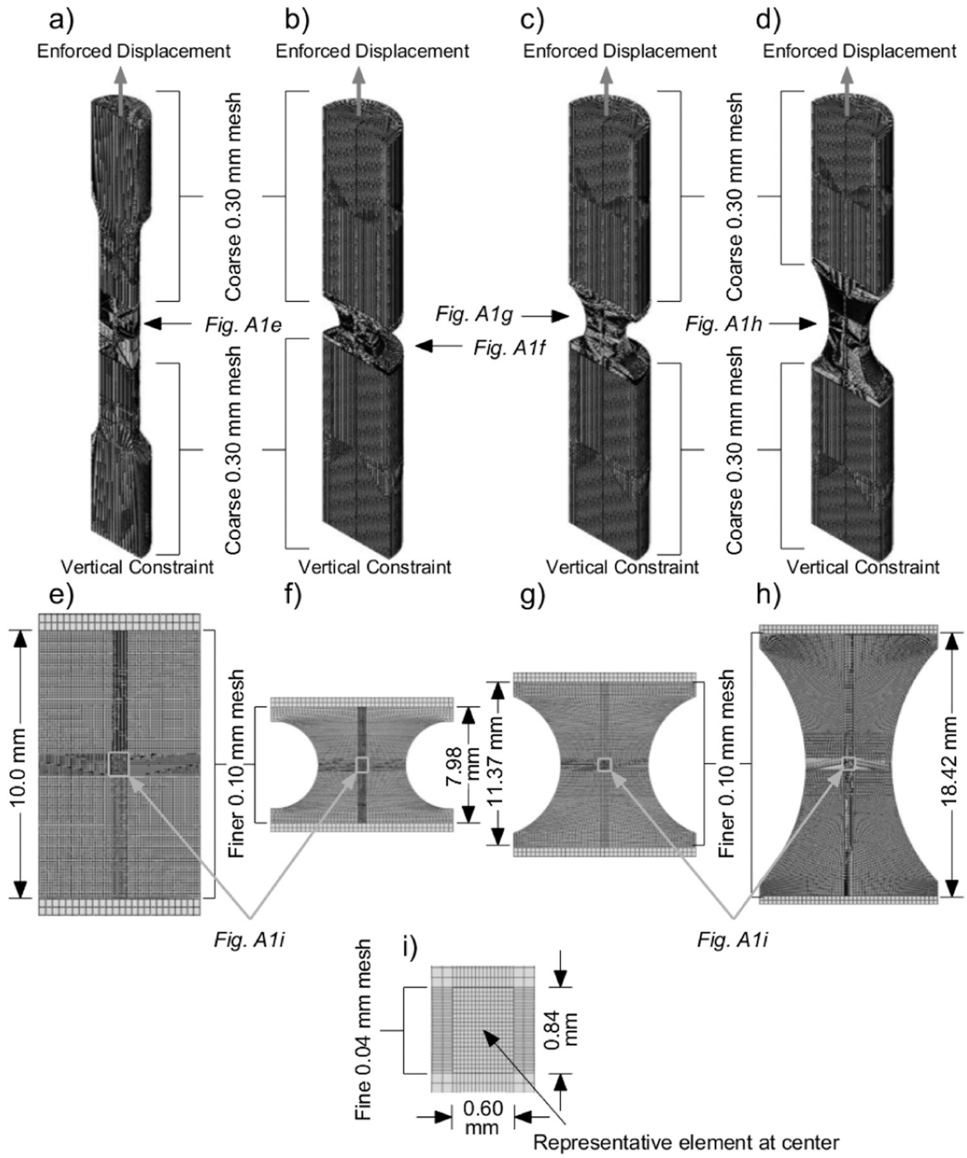

Fig. A1. Isometric views of (a) UT, (b) R3NT, (c) R5NT, and (d) R12NT finite element models. Front views of gauge region for (e) UT, (f) R3NT, (g) R5NT, (h) R12NT models. (i) The central region's elements are 0.04 mm in edge length, and the stress state is extracted from the centermost element.

References

[1] G. Lütjering, J.C. Williams. Titanium, second ed., Springer, 2007.

[2] H. Shipley, D. McDonnell, M. Culleton, R. Coull, R. Lupoi, G. O'Donnell, D. Trimble, Optimisation of process parameters to address fundamental challenges during selective laser melting of Ti-6Al-4V: a review, Int. J. Mach. Tools Manuf. 128 (2018) 1–20, https://doi.org/10.1016/j.ijmachtools.2018.01.003.

[3] J. Yang, H. Yu, J. Yin, M. Gao, Z. Wang, X. Zeng, Formation and control of martensite in Ti-6Al-4V alloy produced by selective laser melting, Mater. Des. 108 (2016) 308–318, https://doi.org/10.1016/j.matdes.2016.06.117.

[4] L. Facchini, E. Magalini, P. Robotti, A. Molinari, S. Höges, K. Wissenbach, Ductility of a Ti-6Al-4V alloy produced by selective laser melting of prealloyed powders, Rapid Prototyp. J. 16 (2010) 450–459, https://doi.org/10.1108/13552541011083371.

[5] H. Galarraga, D.A. Lados, R.R. Dehoff, M.M. Kirka, P. Nandwana, Effects of the microstructure and porosity on properties of Ti-6Al-4V ELI alloy fabricated by electron beam melting (EBM), Addit. Manuf. 10 (2016) 47–57, https://doi.org/10.1016/j.addma.2016.02.003.

[6] G. Kasperovich, J. Haubrich, J. Gussone, G. Requena, Correlation between porosity and processing parameters in TiAl6V4 produced by selective laser melting, Mater. Des. 105 (2016) 160–170, https://doi.org/10.1016/j.matdes.2016.05.070.

[7] R. Rai, J.W. Elmer, T.A. Palmer, T. Debroy, Heat transfer and fluid flow during keyhole mode laser welding of tantalum, Ti-6Al-4V, 304L stainless steel and vanadium, J. Phys. D. Appl. Phys. 40 (2007) 5753–5766, https://doi.org/10.1088/0022-3727/40/18/037.

[8] J.D. Madison, L.K. Aagesen, Quantitative characterization of porosity in laser welds of stainless steel, Scr. Mater. 67 (2012) 783–786, https://doi.org/10.1016/j.scriptamat.2012.06.015.

[9] T. Ronneberg, C.M. Davies, P.A. Hooper, Revealing relationships between porosity, microstructure and mechanical properties of laser powder bed fusion 316L stainless steel through heat treatment, Mater. Des. 189 (2020), 108481, https://doi.org/10.1016/j.matdes.2020.108481.

[10] Y.N. Hu, S.C. Wu, P.J. Withers, J. Zhang, H.Y.X. Bao, Y.N. Fu, G.Z. Kang, The effect of manufacturing defects on the fatigue life of selective laser melted Ti-6Al-4V structures, Mater. Des. 192 (2020), 108708, https://doi.org/10.1016/j.matdes.2020.108708.

[11] L.X. Meng, D.D. Ben, H.J. Yang, H.B. Ji, D.L. Lian, Y.K. Zhu, J. Chen, J.L. Yi, L. Wang, J.B. Yang, Z.F. Zhang, Effects of embedded spherical pore on the tensile properties of a selective laser melted Ti6Al4V alloy, Mater. Sci. Eng. A 815 (2021), 141254, https://doi.org/10.1016/j.msea.2021.141254.

[12] A.E. Wilson-Heid, T.C. Novak, A.M. Beese, Characterization of the effects of internal pores on tensile properties of additively manufactured austenitic stainless steel 316L, Exp. Mech. 59 (2019) 793–804, https://doi.org/10.1007/s11340-018-00465-0.

[13] R. Biswal, X. Zhang, A.K. Syed, M. Awd, J. Ding, F. Walther, S. Williams, Criticality of porosity defects on the fatigue performance of wire + arc additive manufactured titanium alloy, Int. J. Fatigue 122 (2019) 208–217, https://doi.org/10.1016/j.ijfatigue.2019.01.017.

[14] T. Wierzbicki, Y. Bao, Y.W. Lee, Y. Bai, Calibration and evaluation of seven fracture models, Int. J. Mech. Sci. 47 (2005) 719–743, https://doi.org/10.1016/j.ijmecsci.2005.03.003.

[15] A.L. Helbert, X. Feaugas, M. Clavel, Influence of stress triaxiality on the damage mechanisms in an equiaxed α/β Ti-6Al-4V alloy, Metall. Mater. Trans. A Phys. Metall. Mater. Sci. 27 A (1996) 3043–3058, https://doi.org/10.1007/BF02663853.
[16] P.W. Bridgman. Studies in Large Plastic Flow and Fracture, first ed., McGraw-Hill, 1964 https://doi.org/10.4159/harvard.9780674731349.
[17] M.W. McElroy, S. Luna, R. Patin, Fracture control for additively manufactured spacecraft structures, in: 70th Int. Astronaut. Congr. (2019) 15. http://biadmin.cibersam.es/Intranet/Ficheros/GetFichero.aspx?FileName=FAST_test.pdf.
[18] 3D Systems, LaserForm® Ti Gr5 (A), 2020, 1–2.
[19] ASTM E8, ASTM E8/E8M standard test methods for tension testing of metallic materials 1, Annu. B. ASTM Stand. 4. (2010) 1–27. https://doi.org/10.1520/E0008.
[20] CorrelatedSolutions, Vic-3D v7 Testing Guide, 2016.
[21] Dassault Systèmes Simulia Corp., Abaqus Analysis User's Guide, (2018).
[22] A.E. Wilson-Heid, S. Qin, A.M. Beese, Anisotropic multiaxial plasticity model for laser powder bed fusion additively manufactured Ti-6Al-4V, Mater. Sci. Eng. A 738 (2018) 90–97, https://doi.org/10.1016/j.msea.2018.09.077.
[23] A. Du Plessis, I. Yadroitsev, I. Yadroitsava, S.G. Le Roux, X-ray microcomputed tomography in additive manufacturing: a review of the current technology and applications, 3D Print. Addit. Manuf. 5 (2018) 227–247, https://doi.org/10.1089/3dp.2018.0060.
[24] J. Huang, Y. Guo, D. Qin, Z. Zhou, D. Li, Y. Li, Influence of stress triaxiality on the failure behavior of Ti-6Al-4V alloy under a broad range of strain rates, Theor. Appl. Fract. Mech. 97 (2018) 48–61, https://doi.org/10.1016/j.tafmec.2018.07.008.
[25] A.E. Wilson-Heid, A.M. Beese, Combined effects of porosity and stress state on the failure behavior of laser powder bed fusion stainless steel 316L, Addit. Manuf. 39 (2021), https://doi.org/10.1016/j.addma.2021.101862.
[26] C. Reinhart, Industrial computer tomography – a universal inspection tool, in: 17th World Conf. Nondestruct. Test., 2008, pp. 25–28.